Three-beam model for studying dislocations in wave pulses

1987 J. Phys. A: Math. Gen. 20 4673

(http://iopscience.iop.org/0305-4470/20/14/013)

J. Phys. A: Math. Gen. **20** (1987) 4673-4696. Printed in the UK

Three-beam model for studying dislocations in wave pulses

K W Nicholls and J F Nye

H H Wills Physics Laboratory, University of Bristol, Tyndall Avenue, Bristol BS8 1TL, UK

Received 17 February 1987

Abstract. A model pulsed wavefield is presented that enables the behaviour of the associated wave dislocations to be computed exactly. It consists of three intersecting beams of plane-wave pulses. Because the results depend essentially only on the relative time delays of the three pulses at any given point the computations have to be done only once, and they are then applicable, by a linear mapping, to any angular arrangement of the three beams. The model produces dislocations showing the most general behaviour: they are curved, with varying edge-screw character, and they glide and climb. The predictions of the theory of Wright and Nye, valid for small bandwidth but not rigorously justified, are shown to be correct for this model. As the bandwidth increases new dislocation behaviour becomes evident: for example, the dislocation trajectories change their connectivity at or close to saddle points for amplitude in the corresponding continuous-wave pattern. At lower bandwidths Lorentzian-shaped pulses give dislocations that travel on looped trajectories beginning and ending on the nulls of the corresponding continuous-wave pattern, while at higher bandwidths the trajectories lie in close pairs, with one member having small arrival times for the dislocations and the other having large arrival times.

1. Introduction

Generally, pulsed wavefields contain wavefront dislocations (Nye and Berry 1974). These are lines in space along which the amplitude of the complex wavefunction is zero and the phase is consequently undefined. The dislocation lines move to sweep out surfaces called 'dislocation trajectories'. Wavefront dislocations are, in fact, a generalisation of the stationary interference nulls observed in single-frequency wavefields, the positions of the line nulls becoming time dependent when the single-frequency condition is removed by, for example, time modulating the strength of the sources of the waves. An example is given in figure 1 which shows how a dislocation may arise in a two-beam pulsed wavefield. In this case the carrier waves of the two contributory pulses must be in antiphase for a null, which then occurs at any time that the pulse amplitudes are equal (time t_d, for example).

In the same way that the pattern formed by the stationary nulls can be used to characterise a single-frequency wavefield, the dislocation trajectories can, in principle, be used to characterise a pulsed wavefield. The behaviour of wavefront dislocations can be quite complicated (Wright and Berry 1984, Nye 1981, Humphrey 1980) and the calculation of their motion in a realistically complicated wavefield is a lengthy computational task; in fact, most studies so far have used rather simple, and therefore special, models. One which did use a realistic wavefield—that generated by a piston radiator (Wright and Berry 1984)—demonstrated a great diversity of dislocation behaviour but, because of the computational effort required, it was confined to a single pulse shape. A general theory (Wright and Nye 1982) relates the dislocation trajectories

0305-4470/87/144673+24$02.50

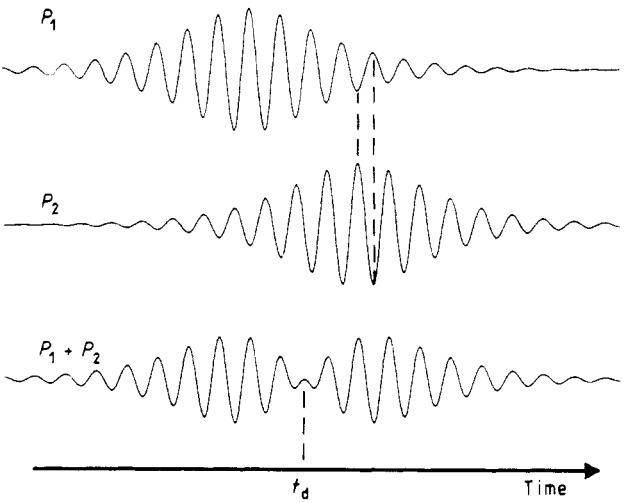

Figure 1. Two identical pulses P_1 and P_2, with a time delay between them, interfere to produce a dislocation at time t_d.

to properties of the corresponding continuous-wave (CW) wavefield, i.e. the wavefield that would exist if the bandwidth of the pulses were reduced to zero. The theory is applicable where the pulses composing the wavefield are the same or simply linearly transformed versions of one original pulse, which itself has only a small bandwidth. In this case, the theoretical prediction is that, to a good approximation, the trajectories of the moving dislocation lines will be parts of the surfaces on which the amplitude of the corresponding CW wavefield is a minimum with respect to variations of CW frequency. The theory also shows how the time of arrival of a dislocation line at a point on its trajectory surface can be found by further analysis of the local CW characteristics together with a knowledge of the shape of the original pulse envelope. This small-bandwidth theory is not entirely rigorous and, as its authors point out, its only ultimate verification comes from comparison with exact results from suitable models. The piston radiator model (Wright and Berry 1984) and laboratory experiments using ultrasonic wavefields (Humphrey 1980, Nicholls and Nye 1986) give results that agree with the theoretical predictions for the positions of the trajectories. Wright and Nye were also able to show that, in a two-beam model, the predicted arrival times for the dislocations were accurate within the small-bandwidth regime and progressively less accurate outside it. However, they further showed that, in any two-beam model, the dislocation trajectories are degenerate in that they always follow exactly the trajectories predicted by the supposedly approximate theory.

This paper describes a model wavefield which contains dislocations exhibiting all the complex behaviour seen before but for which the dislocation behaviour can be computed using simple and efficient numerical techniques. It consists of three identical pulses of plane waves travelling in arbitrary directions and thus is free from the degeneracy inherent in Wright and Nye's two-beam model. It has the great advantage that the computations to derive the motions of the dislocations need be done only once: when they have been done for one set of wave directions the results for any other set of wave directions can be obtained immediately. Although easily computable, therefore, this model represents a complete class of wavefields. Even though the model restricts the wavefield to being composed of only three identical pulses, there is no

restriction on the type of pulse envelope or the pulse bandwidth; in fact, the simplicity of the necessary computations has allowed the calculation of the dislocations for several envelope shapes and bandwidths, thus revealing new behaviour. A further result is to illustrate how the accuracy of the predictions of the small-bandwidth theory, for both dislocation trajectories and arrival times, degrades outside the small-bandwidth regime.

2. The three-beam model

Our model assumes a non-dispersive isotropic homogeneous medium. The three-dimensional wavefield is produced by the interference of three identical pulses of plane waves travelling in different directions (that is, travelling neither parallel nor antiparallel to one another). Each pulse consists of an envelope function $f(t)$ (the 'pulse shape') modulating a carrier wave of frequency ω_0, whose time dependence is taken to be $e^{-i\omega_0 t}$. Thus at the origin $\boldsymbol{r}=0$ each pulse is given by

$$\psi_0(t)=f(t)\,e^{-i\omega_0 t}$$

with $f(t)$ real. At a given point $\boldsymbol{r}$ in the three-dimensional space each wave pulse, say of wavevector $\boldsymbol{k}$, then has the form

$$\psi(t,\tau)=f(t-\tau)\,e^{-i\omega_0(t-\tau)}$$

where τ is the delay time given by $\omega_0\tau=\boldsymbol{k}\cdot\boldsymbol{r}$. Thus the total wavefunction given by the addition of all three pulses is

$$\psi(t;\tau_1,\tau_2,\tau_3)=e^{-i\omega_0 t}[f(t-\tau_1)\,e^{i\omega_0\tau_1}+f(t-\tau_2)\,e^{i\omega_0\tau_2}+f(t-\tau_3)\,e^{i\omega_0\tau_3}] \tag{1}$$

where the three delay times τ_1, τ_2, τ_3 are related to the three wavevectors $\boldsymbol{k}_1$, $\boldsymbol{k}_2$, $\boldsymbol{k}_3$ by

$$\omega_0\tau_1=\boldsymbol{k}_1\cdot\boldsymbol{r} \qquad \omega_0\tau_2=\boldsymbol{k}_2\cdot\boldsymbol{r} \qquad \omega_0\tau_3=\boldsymbol{k}_3\cdot\boldsymbol{r}. \tag{2}$$

Equations (2) can be regarded as defining a linear mapping between $\boldsymbol{r}$ space and τ space, in which a point is defined by its coordinates τ_1, τ_2, τ_3. The mapping is one-to-one, both ways, provided the equations are linearly independent, a condition met in the general case but not when the beams are coplanar (we shall refer to this degenerate case later).

Equation (1) makes no explicit mention of the beam directions. This is important, for it means that, once the wavefield has been determined throughout τ space, the same set of results can be mapped into $\boldsymbol{r}$ space for any configuration of beam directions; all that changes is the mapping.

Inspection of the wavefunction (1) reveals that

$$\psi(t;\tau_1,\tau_2,\tau_3)=\psi(t-T;\tau_1-T,\tau_2-T,\tau_3-T) \tag{3}$$

where T is a constant time delay. This result means that we do not need to compute $\psi(t)$ for all combinations of τ_1, τ_2, τ_3 but only for those lying in a single plane in τ space, for example $\tau_1+\tau_2+\tau_3=0$. To see this, choose T to be the mean delay time $\bar{\tau}=\frac{1}{3}(\tau_1+\tau_2+\tau_3)$ and note that any point (τ_1,τ_2,τ_3) in τ space is then associated by (3) with the point $(\tau_1-\bar{\tau},\ \tau_2-\bar{\tau},\ \tau_3-\bar{\tau})$, which lies in this plane. Thus, as is obvious physically, the form of $\psi(t)$ is decided by the differences in the delay times rather than by their absolute values.

The wavefunction on the plane $\tau_1+\tau_2+\tau_3=0$, which we call the 'reference plane', can be expressed as a function of t and any two of the three delay times τ_1, τ_2, τ_3. Thus, choosing τ_1 and τ_2 it is

$$\psi(t;\tau_1,\tau_2)=e^{-i\omega_0 t}[f(t-\tau_1)\,e^{i\omega_0\tau_1}+f(t-\tau_2)\,e^{i\omega_0\tau_2}+f(t+\tau_1+\tau_2)\,e^{-i\omega_0(\tau_1+\tau_2)}]. \tag{4}$$

The particular features we are interested in are the dislocations, the lines in space where $\psi=0$. From (4), the condition for a dislocation to be present on the reference plane at τ_1, τ_2 and at time t_d is

$$f(t_d-\tau_1)\,e^{i\omega_0\tau_1}+f(t_d-\tau_2)\,e^{i\omega_0\tau_2}+f(t_d+\tau_1+\tau_2)\,e^{-i\omega_0(\tau_1+\tau_2)}=0. \tag{5}$$

In view of (3) with $T=\bar{\tau}$ this is also the condition that a dislocation will be present at the general point (τ_1, τ_2, τ_3) at time $t_d+\bar{\tau}$. In essence, determining the behaviour of dislocations in the three-beam model consists in finding the loci of points at which equation (5) is satisfied.

Since equation (5) is complex it represents two conditions. Elimination of t_d would then yield a relation between τ_1 and τ_2. This is the dislocation trajectory, a line in (τ_1, τ_2) space. As we have explained, the result is applicable to any configuration of the three beams, but to display it in a plane diagram a decision must be made about the reference axes. We choose the system shown in figure 2. Three coplanar reference axes are taken at 120° to one another and the representative point P in the reference plane of τ space with coordinates τ_1, τ_2, τ_3 is located in the plane diagram as the intersection of the three lines perpendicular to the axes whose perpendicular distances from the origin are $\omega_0\tau_1, \omega_0\tau_2, \omega_0\tau_3$. The condition $\tau_1+\tau_2+\tau_3=0$ on the reference plane ensures that the three lines meet in a single point. An advantage of this way of plotting is that the resulting diagram has a simple interpretation in $\boldsymbol{r}$ space, namely it corresponds to three coplanar beams at 120° to one another propagating along the axes. Thus, although the result is applicable by use of the mapping (2) to a general configuration of beams, as we have emphasised, the diagrams we present can also be thought of in this simple way.

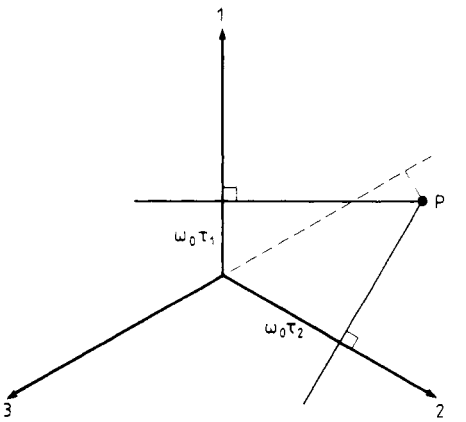

Figure 2. The reference plane $\tau_1+\tau_2+\tau_3=0$ in τ space. The point P has coordinates τ_1, τ_2, τ_3. Interpreted in $\boldsymbol{r}$ space, P lies at the intersection of three wavefronts perpendicular to the three axes.

When the three beams are coplanar, but not necessarily at 120° to one another, there is a linear relation (in general, irrational) between the three wavevectors $\boldsymbol{k}_1, \boldsymbol{k}_2, \boldsymbol{k}_3$:

$$p\boldsymbol{k}_1 + q\boldsymbol{k}_2 + s\boldsymbol{k}_3 = 0$$

where p, q, s are constants. Equations (2) are then no longer linearly independent and, as a consequence, the mapping from $\boldsymbol{r}$ space to τ space is degenerate. In fact the whole of $\boldsymbol{r}$ space then maps onto a single plane in τ space, defined by $p\tau_1 + q\tau_2 + s\tau_3 = 0$. There is no difficulty about this, because we can in principle obtain results covering the whole of τ space. The case of three equally inclined coplanar beams referred to above is the special instance where $p = q = s = 1$, and where the relevant plane in τ space into which $\boldsymbol{r}$ space maps happens also to be the reference plane, defined earlier as $\tau_1 + \tau_2 + \tau_3 = 0$.

Before presenting the pulse results in this way, which is the main object of this paper, we shall describe the dislocation trajectories predicted for the three-beam model by the small-bandwidth theory.

3. The predicted dislocation trajectories

Application of the small-bandwidth theory requires a knowledge of the corresponding continuous-wave (CW) wavefield ψ_{CW} in the neighbourhood of the pulse centre frequency ω_0. This is constructed by allowing the three beams to be of frequency ω and unit amplitude. The wavevectors are now $\boldsymbol{K}_1 = (\omega/\omega_0)\boldsymbol{k}_1$, $\boldsymbol{K}_2 = (\omega/\omega_0)\boldsymbol{k}_2$, $\boldsymbol{K}_3 = (\omega/\omega_0)\boldsymbol{k}_3$ and we have

$$\psi_{CW} = (e^{i\phi_1} + e^{i\phi_2} + e^{i\phi_3})\, e^{-i\omega t} \tag{6}$$

where $\phi_1 = \boldsymbol{K}_1 \cdot \boldsymbol{r}$, $\phi_2 = \boldsymbol{K}_2 \cdot \boldsymbol{r}$, $\phi_3 = \boldsymbol{K}_3 \cdot \boldsymbol{r}$. The complex amplitude of this CW wavefield is denoted by $a(\boldsymbol{r}, \omega)$. Thus

$$a(\boldsymbol{r}, \omega) = e^{i\phi_1} + e^{i\phi_2} + e^{i\phi_3}. \tag{7}$$

For given frequency this is a three-dimensional distribution of amplitude and phase and we need a suitable two-dimensional display. Choosing frequency ω_0 the phases are simply

$$\phi_1 = \boldsymbol{k}_1 \cdot \boldsymbol{r} \qquad \phi_2 = \boldsymbol{k}_2 \cdot \boldsymbol{r} \qquad \phi_3 = \boldsymbol{k}_3 \cdot \boldsymbol{r} \tag{8}$$

which is the same as (2) with $\omega_0\tau_1$, $\omega_0\tau_2$, $\omega_0\tau_3$ replaced by ϕ_1, ϕ_2, ϕ_3. We therefore proceed just as for the pulse case.

For fixed frequency the complex amplitude a can be regarded either as a function of position $\boldsymbol{r}$ or of the phases ϕ_1, ϕ_2, ϕ_3. Then, noting that

$$a(\phi_1, \phi_2, \phi_3) = e^{i\Phi} a(\phi_1 - \Phi, \phi_2 - \Phi, \phi_3 - \Phi) \tag{9}$$

and taking the constant Φ to be the mean phase $\frac{1}{3}(\phi_1 + \phi_2 + \phi_3)$, we can refer all results to the plane in ϕ space $\phi_1 + \phi_2 + \phi_3 = 0$, which, by the mappings (2) and (8), is the reference plane.

We write M for the modulus of a, i.e. the amplitude of the continuous wave. Equation (9) shows that adding a constant to all the phases leaves M unaltered, and therefore the amplitude pattern remains constant in ϕ space on lines parallel to $\phi_1 = \phi_2 = \phi_3$—that is to say, in $\boldsymbol{r}$ space on lines parallel to $\boldsymbol{k}_1 \cdot \boldsymbol{r} = \boldsymbol{k}_2 \cdot \boldsymbol{r} = \boldsymbol{k}_3 \cdot \boldsymbol{r}$. This is parallel to the vector $\boldsymbol{k}_2 \times \boldsymbol{k}_3 + \boldsymbol{k}_3 \times \boldsymbol{k}_1 + \boldsymbol{k}_1 \times \boldsymbol{k}_2$ which we call the 'pattern axis'. (It is

not, in general, perpendicular to the reference plane in $\boldsymbol{r}$ space.) Thus the amplitude pattern for ψ_{CW}, unlike the phase pattern, is essentially two dimensional. We represent it in the plane $\phi_1+\phi_2+\phi_3=0$ by drawing a diagram exactly analogous to figure 2, with $\omega_0\tau_1$, $\omega_0\tau_2$, $\omega_0\tau_3$ replaced by ϕ_1, ϕ_2, ϕ_3. The diagram can be read in two ways: (*a*) it is the amplitude pattern in $\boldsymbol{r}$ space for three coplanar beams at 120°; (*b*) after linear distortion given by the mapping (8) it is the amplitude pattern in $\boldsymbol{r}$ space for three beams inclined at general angles.

The prediction of the small-bandwidth theory is that to first order the dislocation trajectories are parts of the surfaces defined by

$$\left(\frac{\partial M}{\partial \omega}\right)_{\omega=\omega_0}=0 \qquad \left(\frac{\partial^2 M}{\partial \omega^2}\right)_{\omega=\omega_0}>0 \tag{10}$$

i.e. frequency minima of the amplitude. In the three-beam model, where the beams remain of unit amplitude, by equation (6), changing the frequency simply changes the scale of the pattern in ϕ space and $\boldsymbol{r}$ space. The surfaces given by (10) are called potential trajectories and are independent of the pulse shape. It is predicted that the dislocation lines sweep out only parts of these surfaces, and that the pulse shape determines the precise extent to which they are used by the dislocations.

The full phase and amplitude pattern of ψ_{CW} is given in appendix 1. Here we need only the amplitude pattern for $\omega=\omega_0$ and the surfaces given by (10), which are shown in figure 3. Because of the symmetry the full pattern can be inferred from one 30° sector. The bolder full lines are the loci for which both of equations (10) hold; the broken lines indicate those additional loci (maxima) for which only the first is true. The lighter background lines are the contours of amplitude. From the figure it appears that the potential trajectories include all the CW null lines and selected saddles for CW amplitude. The potential trajectory surfaces will always include the null lines but it is a special property of the three-beam model that causes saddles to be included as well. The potential trajectory is the locus of points where the amplitude does not change under an infinitesimal change of frequency. Therefore only if the amplitude at a saddle stays unchanged does it lie on the potential trajectory. In the three-beam model this condition is fulfilled because varying the frequency simply changes the spatial scale of the amplitude pattern. In a general wavefield, unlike this one, the

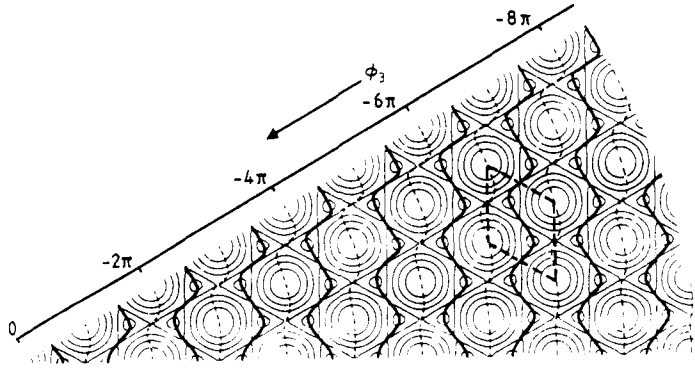

Figure 3. The CW amplitude pattern for $\omega=\omega_0$ (light contours). A unit cell is outlined. The small-bandwidth theory predicts that the pulse dislocations will move along parts of the bold lines, given by equations (10). The nulls of the amplitude pattern are indicated by circular contours centred on the bold lines; the other circular contours denote maxima. The trajectory pattern is not periodic.

numbers and directions of the constituent plane waves would vary with frequency and therefore both the positions and the heights of saddles would do so too.

The potential dislocation trajectories are concentric corrugated cylinders lying parallel to $\phi_1 = \phi_2 = \phi_3$ in ϕ space, or in $\boldsymbol{r}$ space the pattern axis. If figure 3 is thought of as representing the case of three coplanar beams at 120°, the cylinders are perpendicular to the diagram. We will show later how the small-bandwidth theory determines what portions of the potential trajectories are used by the dislocations, and the way this is affected by pulse shape.

4. The computed trajectories and times of the dislocations

We now outline the method used to find the loci on which the dislocation condition (5) is satisfied, i.e. the method used to compute the dislocation trajectories exactly. First, a pulse envelope function $f(t)$ must be chosen and, following Wright and Nye (1982), we take as our main example $f(t) = \operatorname{sech}(\sigma t)$, where σ is the bandwidth of the pulse (figure 4). Then we decompose the dislocation condition (5) into its real and imaginary components, namely

$$\begin{aligned}
&\operatorname{sech}\sigma(t-\tau_1)\cos\omega_0\tau_1 + \operatorname{sech}\sigma(t-\tau_2)\cos\omega_0\tau_2 \\
&\qquad + \operatorname{sech}\sigma(t+\tau_1+\tau_2)\cos\omega_0(\tau_1+\tau_2) = 0 \\
&\operatorname{sech}\sigma(t-\tau_1)\sin\omega_0\tau_1 + \operatorname{sech}\sigma(t-\tau_2)\sin\omega_0\tau_2 \\
&\qquad - \operatorname{sech}\sigma(t+\tau_1+\tau_2)\sin\omega_0(\tau_1+\tau_2) = 0.
\end{aligned} \tag{11}$$

For a point (τ_1, τ_2) near a dislocation trajectory the real and imaginary parts will generally pass through zero at different times t_r and t_i, as shown in figure 5. To find a locus for which (11) is satisfied, we select a point (τ_1, τ_2) that lies on a potential dislocation trajectory (and, we hope, near an actual trajectory) and then use a simple approximation algorithm to find the times of the zero crossings. If the point is indeed near a dislocation trajectory the interval between t_r and t_i will be small. By adjusting the position (modifying either τ_1 or τ_2) and monitoring the effect of these adjustments on the recalculated time interval, we can reduce the interval to zero. Condition (11) is then satisfied: the time t_d of the (simultaneous) zero crossings is the time of arrival of a dislocation at a point on its trajectory corresponding to the final values of τ_1 and τ_2. The triplet (τ_1, τ_2, t_d) is stored.

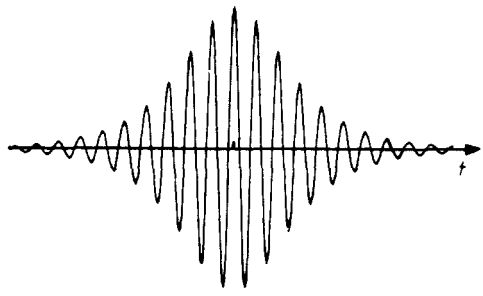

Figure 4. A single hyperbolic secant pulse ($\sigma = 0.073\omega_0$) with the carrier wave, as it would be seen on an oscilloscope.

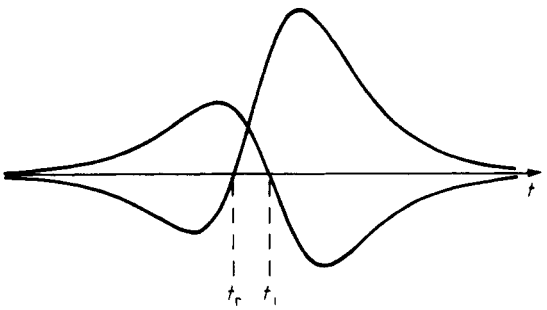

Figure 5. The real and imaginary parts of the complex amplitude of the signal at a given position near a dislocation trajectory. The zeros occur at times t_r and t_i respectively.

A neighbouring point on the dislocation trajectory may be found by stepping either τ_1 or τ_2 and then repeating the search procedure. In this way the complete trajectory can be traced out, the search algorithm only failing when the gradients of the real and imaginary parts of the received pulse are both small in the vicinity of the zero crossings, a condition which arises when the dislocation is in the far head or tail of the pulse. To deal with this we introduce an arbitrary visibility threshold. The numerically simple and computationally economical nature of this method of determining the dislocation arrival times and trajectories is the most important advantage of the model: it has made it feasible to calculate the dislocation behaviour in a wavefield using several types of pulse envelope (hyperbolic secant, Gaussian, Lorentzian and a non-symmetric curve) at many different bandwidths σ.

Inspection of conditions (11) reveals invariance under the transformations

$$(\tau_1, \tau_2, \tau_3) \rightarrow (\tau_2, \tau_3, \tau_1) \qquad \tau_3 = -\tau_1 - \tau_2$$

$$(\tau_1, \tau_2, t) \rightarrow (-\tau_1, -\tau_2, -t)$$

$$(\tau_1, \tau_2) \rightarrow (\tau_2, \tau_1).$$

In the plane diagram described in § 2 this implies a threefold rotation axis through the origin, a time-reversing diad axis also through the origin and a mirror line along $\tau_1 = \tau_2$. Thus we need to find the dislocation trajectories for only a 30° sector of the wavefield and can use graphical manipulation to generate the full 360° pattern. Figure 6(a) shows the dislocation trajectories in the three-beam model for a bandwidth of $0.073\omega_0$ (that is, using a pulse envelope $f(t) = \mathrm{sech}(0.073\omega_0 t)$) out to a radius of about 5 periods of the carrier wave. Figure 6(b) shows one 60° sector of the pattern with the motion of the dislocations indicated.

In viewing this pattern we should keep in mind that it is for the reference plane $\tau_1 + \tau_2 + \tau_3 = 0$ in τ space or, by the mapping (2), for the plane $(\boldsymbol{k}_1 + \boldsymbol{k}_2 + \boldsymbol{k}_3) \cdot \boldsymbol{r} = 0$ in $\boldsymbol{r}$ space. Thus the computed dislocation arrival times are those appropriate to this plane. It is easiest to visualise the case where the three beams are coplanar at 120° to one another. Then the diagram simply represents a plane in $\boldsymbol{r}$ space perpendicular to the dislocations and the arrival times are those appropriate to this transverse plane.

The pattern in figure 6(a) has three distinct regions: the 'inner region' containing disconnected trajectories, the 'intermediate region' in which the trajectories have connected into rings and the 'outer region' where sets of trajectories cross each other. The connectivity of the trajectories in the outer region is established by looking at the arrival times of the dislocations. A given segment of trajectory can then be of two

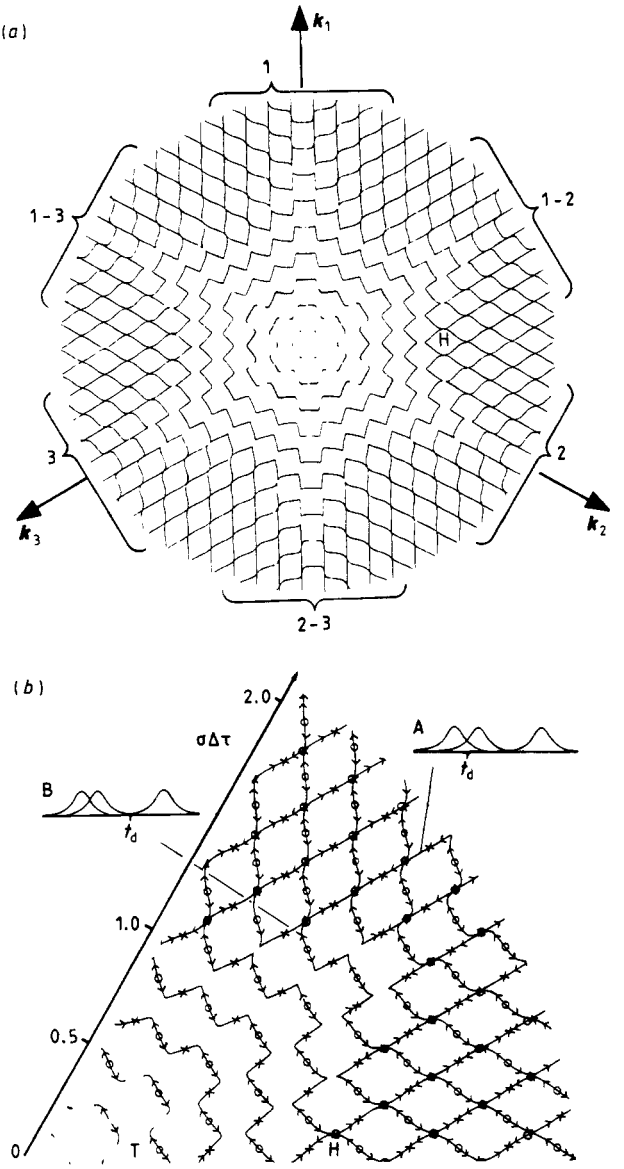

Figure 6. (*a*) Computed dislocation trajectories in the reference plane for a hyperbolic secant pulse envelope ($\sigma = 0.073\omega_0$). The $\boldsymbol{k}$ vectors shown refer to the case of three coplanar beams at 120° to one another. (*b*) A 60° sector, with arrowheads showing the direction of motion of the dislocations. They collide and annihilate at the positions marked × and are born in pairs at the positions marked ○. H is the site of the hooking-up event shown in detail in figure 8. At junctions each trajectory runs straight across.

kinds: (i) almost straight and tending to lie radially, and (ii) a remnant of the trajectory rings, zigzagging around the intermediate region. The first kind corresponds to interference essentially between only two pulses (figure 6(*b*) inset A); the third pulse is so distant in time that its far head or tail acts merely as a perturbation. We call these 'two-beam' segments. The second kind of segment corresponds to the far head or tail

of a distant pulse generating a dislocation by interfering with the combined tails or heads of the other two (figure 6(*b*) inset B), which we call 'three-beam' segments. At points where trajectory segments of the two types cross the two configurations occur at different times in the same received pulse. Further from the intermediate region, as the third pulse becomes more separated, the visibility of dislocations on the three-beam segments deteriorates and they become progressively more difficult to track numerically; this sets a radial limit on the calculated pattern. From figure 6(*a*) it can be seen that the two-beam segments gradually feel more of the third pulse as they approach the intermediate region, where they turn into three-beam segments.

A convenient way of showing the motion of the dislocations is to plot their arrival time t_d as a function of distance s along the trajectory (from some arbitrary origin). Figure 7 illustrates the typical motion of dislocations found in (*a*) the inner, (*b*) the intermediate and (*c*) the outer regions. Maxima of t_d represent dislocations colliding and annihilating; minima correspond to pairs of dislocations being created and then separating. Figure 7(*c*) shows a cascade of annihilations and pair creations: at A a dislocation annihilates with one of a pair created further along the trajectory (at B). The second of the pair proceeds along the trajectory, effectively replacing the original dislocation, and the sequence is repeated. Wright and Berry (1984), who saw dislocations with similar behaviour in their piston radiator model, called each annihilation-creation couplet a 'skip' event.

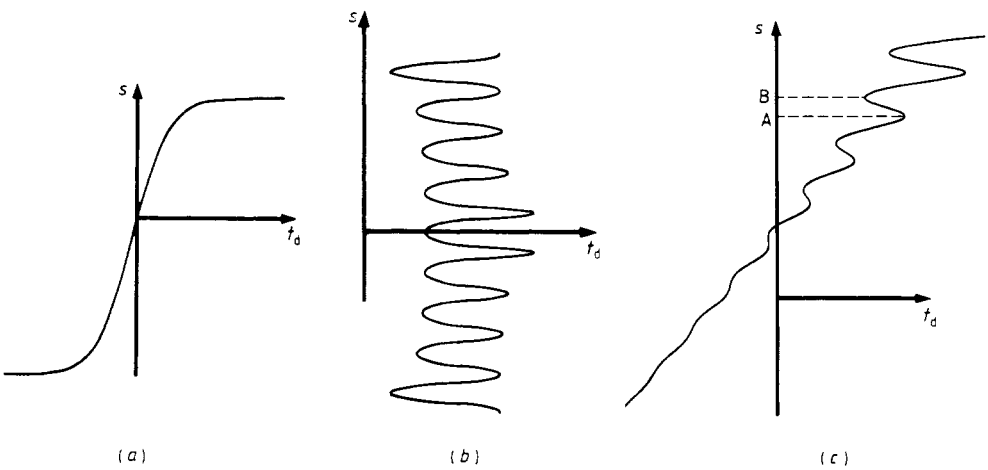

Figure 7. Typical motions of dislocations shown by plotting distance s along the trajectory against arrival time t_d. (*a*) Inner region, (*b*) intermediate region, (*c*) outer region.

We can now describe in general terms the history of the dislocations in the pulsed model. Very early, before the main part of any of the pulses has arrived at the origin, dislocations are present only in the inner region, and far out in sectors 1, 2 and 3 (figure 6(*a*)). Those in the inner region are generated by the far heads of the pulses and, as can be seen from figure 7(*a*), travel very slowly at first. In the outer region, however, the dislocations are produced by the interference of the main parts of only two pulses and move rigidly with the composite wave at a speed of $2c$ (in the coplanar 120° beam configuration), c being the plane-wave velocity. As these dislocations approach the intermediate region they begin to feel the effect of the third pulse, and their speed begins to vary (figure 7(*c*)) to the extent that they eventually skip. At about

this time pairs of dislocations are born in sectors 1, 2 and 3 of the intermediate region, skipping round the central region until they meet the boundary of their sectors, where they annihilate with others engaged in the same activity in neighbouring sectors. In the intermediate region, therefore, dislocations exist for a well defined and limited period of time. The dislocations in the inner region have now accelerated to their maximum speed and are passing near their associated CW nulls (i.e. the positions they condense onto as the bandwidth of the original pulses is reduced to zero). The incoming dislocations in the outer region are ultimately either turned away through 60° or, after skipping around the intermediate region, are turned away to leave at an angle of 120° to their original directions. At very much later times, well after the main parts of all the pulses have passsed through the origin, the only surviving dislocations are those, once again, moving very slowly in the inner region, and others retreating far out in sectors 1-2, 2-3 and 1-3.

5. Variation with bandwidth

We now examine how the behaviour of the dislocations changes with bandwidth. This is important because it is the size of the bandwidth that limits the accuracy of Wright and Nye's theory. They have shown that the dimensionless parameter which characterises how much a pulsed wavefield differs from a continuous wavefield is the 'delay-bandwidth', $\sigma\Delta\tau$, where $\Delta\tau$ is the 'elongation time' of the observed pulse ($\Delta\tau_1$ in their notation). The elongation time is a measure of the spread in arrival times of the individual pulses constituting the received signal.

In the three-beam model a convenient measure of elongation time is the root-mean-square delay of the three pulses with respect to their mean delay $\bar{\tau} = \frac{1}{3}(\tau_1 + \tau_2 + \tau_3)$, which is zero on the reference plane. On that plane, therefore, the delay bandwidth $\sigma\Delta\tau$ is $\sigma[\frac{2}{3}(\tau_1^2 + \tau_2^2 + \tau_1\tau_2)]^{1/2}$. It is easy to show that, on diagrams such as those in figures 6(a, b), there is a linear increase in $\sigma\Delta\tau$ with radial distance from the origin, independent of the azimuthal angle. We can say, then, that the wavefield resembles continuous waves nearer the origin, and becomes more pulse-like further from the origin. In effect, the bandwidth scales the delay times. With a decreased bandwidth σ the delay times must be increased to show the pulsed nature of the wavefield to the same degree. Thus the sizes of the intermediate and inner regions of the pattern in figure 6(a) can be changed by changing σ. The extreme of low bandwidth is of course the CW case, the pattern consisting of a hexagonal array of dots at the CW null positions. In this case the inner region has spread over the entire plane. In the extreme of large bandwidth the pattern would, in theory, consist of a lattice of straight lines, the two-beam-dominated far-field now stretching into the origin. In practice the visibility of the dislocations would be so low as to make them undetectable, because they would result from the mutual cancellation of very low-amplitude parts of the pulse envelopes.

The change in delay-bandwidth with radial displacement is a useful feature of the three-beam model, and of the coplanar symmetric beam configuration in particular; a single figure can be used to show the change in structure of the dislocation trajectories as $\sigma\Delta\tau$ is varied. Of course, in this presentation trajectories are shown only for discrete values of delay-bandwidth, and so fine details of their change in form with σ will be missed.

A phenomenon of this kind is the hooking-up of trajectory rings, seen, for example, near H in figures 6(a, b). To investigate its details the trajectories in the neighbourhood

have to be recalculated for several values of σ in the appropriate range. A sequence of trajectory diagrams is shown in figure 8, illustrating how the outer trajectory forms a loop before connecting with the inner branch. Before the hook-up two dislocations nearly collide and rebound; after it, two dislocations annihilate and then two more are created. At the hook-up itself either description is valid. Nye and Berry (1974) interpreted a point of connection like this as a collision and rebound of dislocations. We see here how such an event is structurally unstable to change in bandwidth. In the range $0.8 < \sigma\Delta\tau < 1.4$ similar hook-ups occur at other points between the intermediate and outer regions.

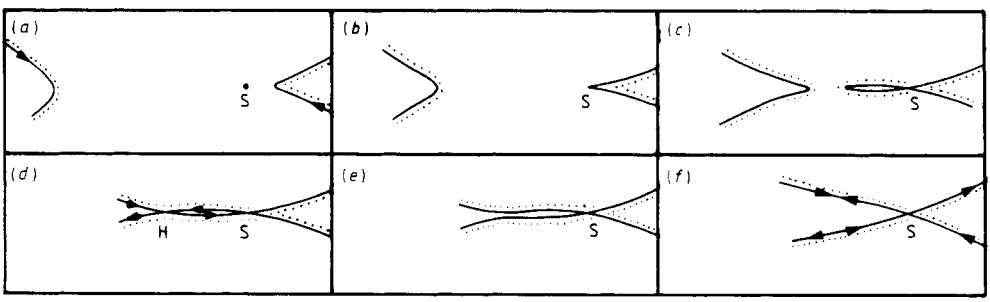

Figure 8. The hooking-up of dislocation trajectories. (*a*)-(*f*) show how the trajectories evolve as the bandwidth is increased. The hook-up occurs at the point H in (*d*) at a delay-bandwidth of $\sigma\Delta\tau = 1.01$. S is a saddle for CW amplitude. Arrows show the direction of motion of dislocations.

Why do the dislocation trajectories form a loop before hooking-up? A physical interpretation may be given by noting that trajectories have a 'sidedness': on one side the received pulse has one more wavecrest than on the other. In figure 8 the sides of the two trajectory branches are distinguished by shading, and the mechanism used in the hook-up can now be seen to ensure that the sides match up after the event. It is interesting that the point where the trajectory crosses itself remains fixed and coincides exactly with a saddle for amplitude in the corresponding CW pattern.

6. Comparison with theory

We next check the agreement between the predictions of the small-bandwidth theory and the computed results, which, as we have emphasised, can be obtained for any bandwidth. A comparison between the computed trajectories (figure 6(*b*)) and the potential trajectories of the small-bandwidth theory (figure 3) shows that in the inner region the dislocations follow segments of the potential trajectories containing CW nulls, in the intermediate region the computed trajectories have the same general form as the potential trajectories but differ from them in detail, while in the outer region there is little correspondence between the two patterns. This is in broad agreement with our expectations of the theory. It is most accurate near the origin where the delay-bandwidth is small and becomes less accurate as the delay-bandwidth increases. It is notable that the only potential trajectories predicted by the small-bandwidth theory in the outer region are those shown by the exact computation to be associated with three-beam events; there are no two-beam potential trajectories.

For more detailed comparisons between the computed results and the predictions of the small-bandwidth theory we select one dislocation trajectory in the pattern and look at the dislocation arrival times along its length. To avoid any special symmetry effects the chosen trajectory (T in figure 6(*b*)) is associated with a CW null which does not lie on a symmetry axis. Wright and Nye (1982) show that for any trajectory

$$M_0' = 0 \qquad M_0'' > 0 \tag{12a}$$

and

$$t_d = \phi_0' + \mathrm{sgn}(\phi_0''')(M_0''/M_0)^{1/2} + \tilde{t} \tag{12b}$$

where $\tilde{t}$ satisfies

$$f(\tilde{t}) + \mathrm{sgn}(\phi_0''')(M_0''/M_0)^{1/2} f'(\tilde{t}) = 0. \tag{12c}$$

Equation (12*a*) was given in § 3 and is the condition for a potential trajectory; the primes indicate differentiation with respect to ω, and the suffix zero indicates that the derivative is evaluated at ω_0. In (12*b*) and (12*c*), ϕ represents the phase of $a(\boldsymbol{r}, \omega)$, t_d is the arrival time of the dislocation and $f'(t)$ is the time derivative of the envelope function $f(t)$. The parts of the potential trajectories (defined by (12*a*)) used by dislocations are those on which the arrival time (given by (12*b*, *c*)) is real.

Figure 9(*a*) shows the potential trajectory (the broken curve) together with the computed trajectories for delay-bandwidths of 0.07, 0.14, 0.29 and 0.43. As the bandwidth is increased, the dislocation trajectories both lengthen and migrate from the CW null position. This migration is not given by the first-order theory, but it is anticipated in a more rigorous approximate theory (Wright and Nye 1982) developed to show dislocation behaviour in the immediate vicinity of CW nulls. This 'local theory' shows that, for small bandwidths, dislocation trajectories are expected to miss the nulls by a distance proportional to the square of the bandwidth, a prediction shown in figure 9(*b*) to be verified for $\sigma\Delta\tau \leqslant 0.2$ by the exact three-beam computation.

Another theoretical result is that the length of dislocation trajectories is directly proportional to the bandwidth. Figure 9(*c*) shows that, in our example, this result is valid for $\sigma\Delta\tau \leqslant 0.4$. It is interesting to notice in figure 9(*a*) how the end portions of the trajectories converge onto the potential trajectory at larger bandwidths and, at the same time, the endpoints approach the saddles for M_0. We recall from § 3 that, in wavefields composed of a fixed set of plane-wave beams whose directions are independent of frequency (such as the three-beam wavefield), those saddles for which $M_0'' \geqslant 0$ are always included in the potential trajectories. It appears that, in the three-beam model, for high enough bandwidth the actual (computed) trajectories are also pinned by these saddles. This cannot be a general property of pulse diffraction patterns because it would imply that the centre frequency ω_0 of the pulse had a special status.

For dislocation arrival times, figure 10 shows close agreement between the first-order small-bandwidth theory and the computed results at least up to $\sigma\Delta\tau = 0.43$. Moreover, some of the divergence from the theory will be due to the difficulty in comparing two quantities on different curved lines (that is, the predicted and computed trajectories). Wright and Nye's local approximate theory gives the arrival time of a dislocation at a special point on its trajectory close to the CW null. This point, J, is the intersection of the trajectory with the line $M = 0$, the line swept out by the CW null as the frequency is varied. (Note that they consider a two-dimensional section through the wavefield, perpendicular to the dislocation line.) Their result is that the time from the first-order small-bandwidth theory at which the dislocation passes through the null is identical

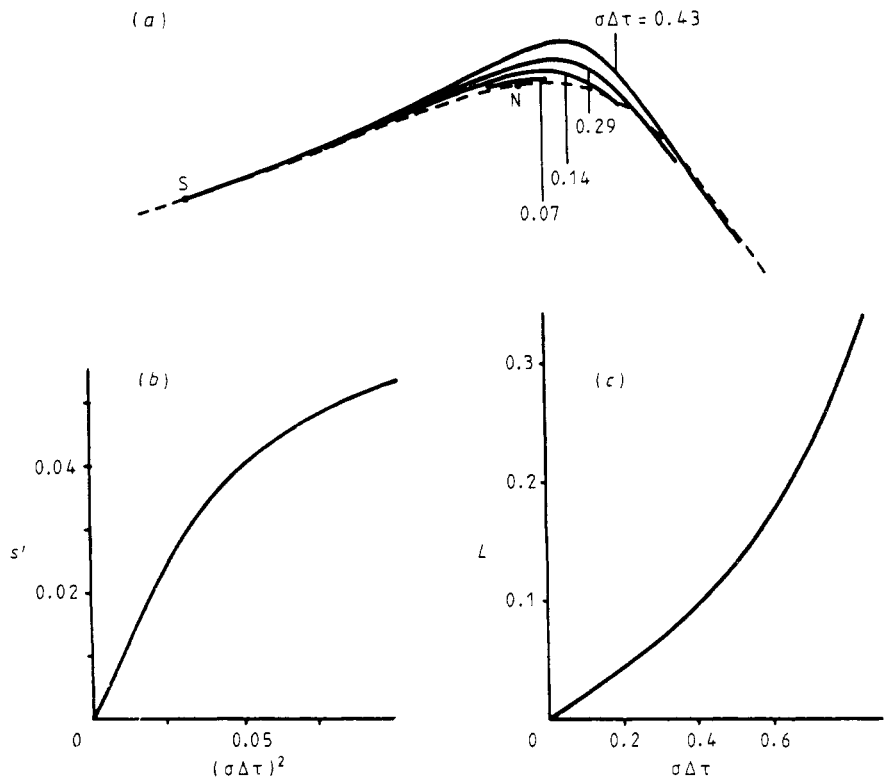

Figure 9. (*a*) Magnified view of the dislocation trajectory marked T in figure 6(*b*), associated with the CW null at $(\omega_0\tau_1, \omega_0\tau_2) = (\frac{4}{3}\pi, \frac{2}{3}\pi)$, for a hyperbolic secant pulse envelope. The potential trajectory (broken curve) joins the saddle point for CW amplitude marked S with another outside the diagram, and passes through the CW null N. The length and position of the actual (computed) trajectory depends on the delay-bandwidth, as shown by the full curves, converging to N as $\sigma\Delta\tau \to 0$. (*b*) Perpendicular distance s' of the trajectory from N plotted against the square of the bandwidth. (*c*) Total length L of the trajectory plotted against the bandwidth.

with the time at which the dislocation passes (more accurately) through J in the local theory. They also show that the speed of the dislocation is constant near the null, a result seen from figure 10 to be accurate for $\sigma\Delta\tau \leqslant 0.3$. Figure 11 shows that even for quite high bandwidths ($\sigma\Delta\tau \sim 0.5$) the prediction for the arrival time at J agrees closely with the numerical results (note the highly expanded arrival-time scale and recall that, in general, arrival times are between $\pm\infty$). The deviation from the theory is accurately quadratic with bandwidth, as would be expected, because changing the sign of σ with a symmetric pulse leaves the physical situation unaltered. When extrapolated back to $\sigma\Delta\tau = 0$, the graph yields the predicted value with great accuracy, thereby not only verifying the theory but also providing a stringent check on our numerical methods.

7. The Lorentzian pulse shape

Wright and Nye's two-beam model showed that the motion of dislocations is very sensitive to the asymptotic behaviour of the head and tail of the original pulse; the

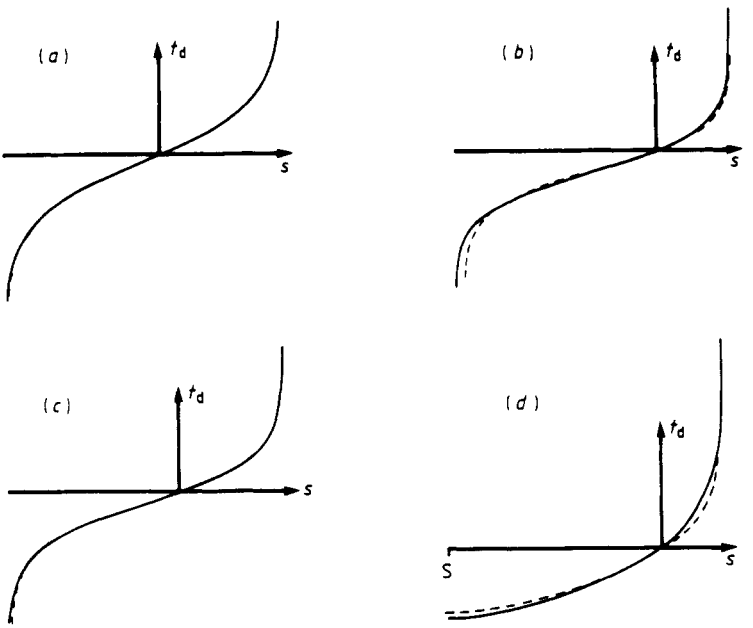

Figure 10. Arrival time t_d as a function of distance s along the trajectory of figure 9(a), for different delay-bandwidths: (a) $\sigma\Delta\tau = 0.07$, (b) 0.29, (c) 0.14, (d) 0.43. The exact (computed) results (full curves) diverge from the predictions of equations (12) (broken curves) as $\sigma\Delta\tau$ increases. The scale for s is not the same in the four diagrams. The shape of the curves in (d) is different because the trajectory has joined up with the adjacent one at a saddle S.

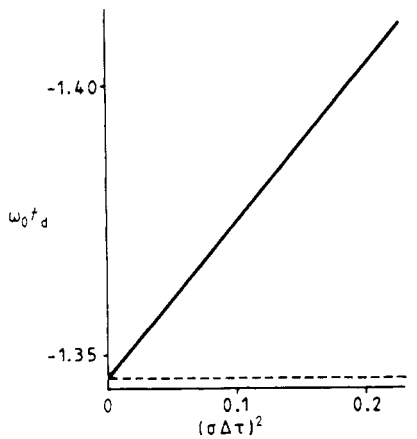

Figure 11. Arrival time t_d at the special point J as a function of $(\sigma\Delta\tau)^2$. The prediction of the local theory (broken line) is very accurately verified as $\sigma\Delta\tau \to 0$.

envelopes of their example pulses were the Gaussian, the hyperbolic secant and the Lorentzian, which decay as e^{-t^2}, e^{-t} and t^{-2} respectively. In §§ 4–6 we have considered the detailed behaviour of dislocations in the three-beam model with the hyperbolic secant pulse envelope. Now we consider the Lorentzian.

In the two-beam model the trajectories for the Lorentzian were similar to those for the hyperbolic secant, consisting of straight disconnected lines through the CW nulls.

However, the time behaviour of the dislocations was more complicated. They started at the CW nulls at time $t = -\infty$, travelled to one end of their trajectory, turned back to travel through the null to the other end, and then returned once again to the null at $t = +\infty$. The trajectories computed for a Lorentzian pulse envelope (with $\sigma = 0.073\omega_0$) in the three-beam model are presented in figure 12(*a*). At first sight the pattern looks very similar to the corresponding one for the hyperbolic secant (figure 6(*a*)). However, figure 12(*b*) is an enlarged section showing the loop structure of a typical disconnected trajectory in the inner region: the folded trajectory found in the two-beam model has, in the three-beam model, opened out. Although we show the ends of the trajectory connected at the CW null, this cannot be determined from the computer program. This is because the visibility of the dislocations becomes lower and lower as the null is approached, and they cannot be tracked all the way. Nevertheless, we assume for now that such trajectories do indeed start and end on their associated CW nulls.

As the delay-bandwidth is increased neighbouring trajectories link up, as near L in figure 12(*a*). Two separate branches are then formed (figure 13), one (broken line) which includes the CW null positions, and on which the arrival times are very late and very early, corresponding to dislocations in the far head and tail, and the other (full line) with more moderate arrival times, corresponding to high-visibility dislocations in the middle of the pulse. The high-visibility branch is reminiscent of the trajectories in the intermediate region of the pattern for the hyperbolic secant; the low visibility

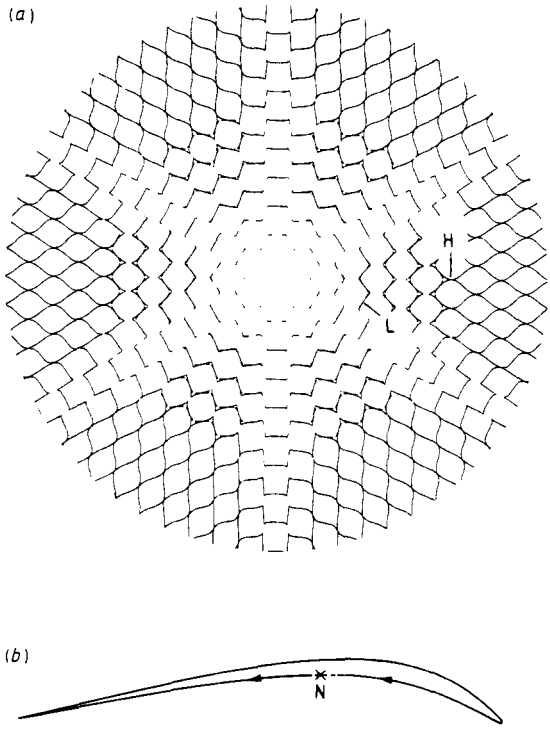

Figure 12. (*a*) Computed three-beam trajectories in the reference plane for a Lorentzian pulse envelope ($\sigma = 0.073\omega_0$). Trajectories towards the centre that appear as a single line are actually double. A typical link-up occurs near L and a typical hook-up near H. (*b*) Magnified view of a trajectory in the inner region; the dislocation starts and finishes at the CW null N.

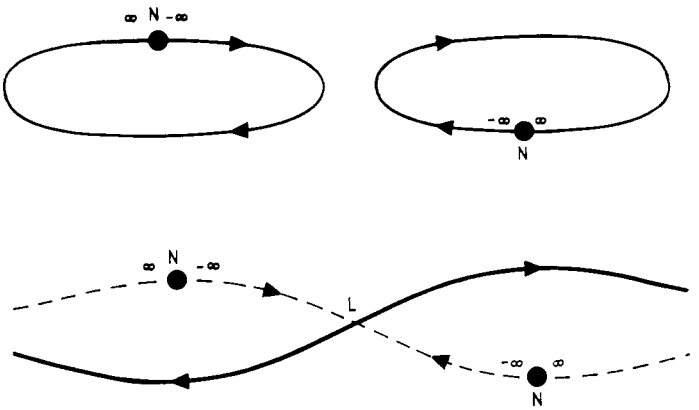

Figure 13. Schematic diagram for a Lorentzian pulse envelope, showing how two disconnected looped trajectories link up at L to produce one branch that contains the nulls N and one that does not. Extreme values of arrival time are shown. The vertical separation is exaggerated.

branch is new. The link-up occurs at saddles in the amplitude of the corresponding CW pattern. It corresponds to the rather simpler link-up noted in § 4 for the hyperbolic secant pulse, where the ends of the trajectories simply joined together to form a single trajectory.

A second way in which trajectories join together is seen near H in figure 12(*a*); this is the hook-up event already described for the hyperbolic secant pulse (figure 8) and it takes place in the same way for both kinds of pulse envelope.

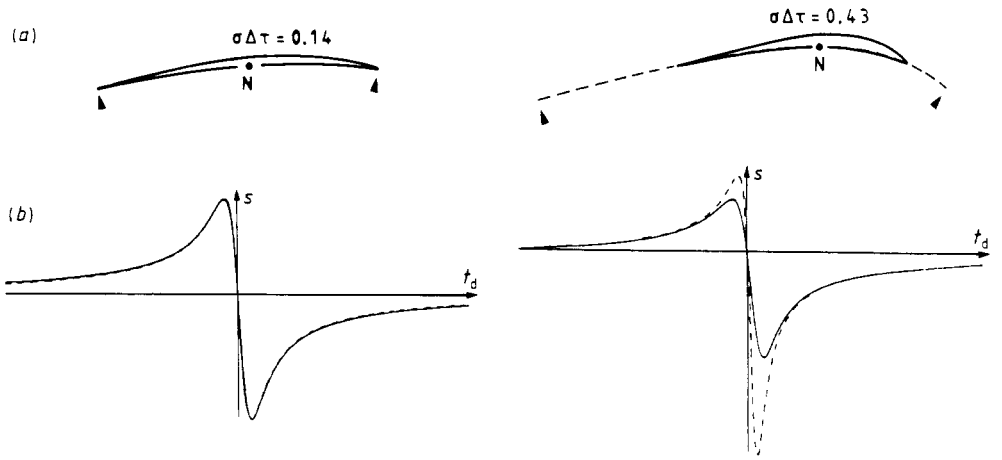

Figure 14. (*a*) Trajectories associated with the CW null N at $\omega_0\tau_1 = \frac{4}{3}\pi$, $\omega_0\tau_2 = \frac{2}{3}\pi$, for a Lorentzian pulse envelope and two different delay-bandwidths. For $\sigma\Delta\tau = 0.43$ the lower part of the computed loop (full curve) lies on the trajectory predicted by the small-bandwidth theory (broken curve terminating at the arrowheads) but its endpoints are different. For $\sigma\Delta\tau = 0.14$ the lower part of the computed loop is indistinguishable from the trajectory predicted by the small-bandwidth theory. (*b*) Distance s along the trajectories in (*a*) plotted against dislocation arrival times t_d. s is measured from the perpendicular to the trajectory through N.

As before, to test the small-bandwidth theory we choose an unsymmetrically placed CW null and compute the associated dislocation trajectory and arrival times for different delay-bandwidths. The results are then compared with those predicted by the first-order theory in equations (12). Figure 14(*a*) shows the computed trajectories for $\sigma\Delta\tau = 0.14$ and 0.43, compared with the trajectories predicted by the first-order theory (broken line). Figure 14(*b*) presents the predicted and computed dislocation arrival times for the same delay-bandwidths. The agreement with the first-order theory is good for the smaller delay-bandwidth for both the trajectory and the arrival times; for the larger value, however, the predictions break down. The loss of accuracy with increased delay-bandwidth is noticeably faster for the Lorentzian than for the hyperbolic secant.

Using Wright and Nye's more rigorous local theory, valid near the nulls, it can be shown that dislocations start and end on nulls exactly as we assumed in figure 12(*b*). This result, which is independent of the bandwidth, appears physically rather odd. Why should dislocations in a wavefield which may have a very high bandwidth be restricted to passing through points which become less significant as the bandwidth is increased? The answer is that, far enough from the centre of a Lorentzian envelope, the rate of change in the amplitude of the envelope is small enough for the beam to resemble continuous waves. This is not so for the hyperbolic secant where the die-away in the envelope remains exponential, and the beam therefore pulse-like, however far from the pulse centre it is observed.

8. Three dimensions

So far the only physical interpretation of the various diagrams we have offered has been in terms of the symmetric coplanar configuration of beam directions. In this section we describe the way the behaviour and form of the dislocation lines change when a three-dimensional configuration is adopted. Recall from § 2 that, once the trajectories and arrival times of the dislocations have been calculated across one plane in τ space (we chose the reference plane $\tau_1 + \tau_2 + \tau_3 = 0$), the same results can be interpreted for any configuration of beam directions. Thus, for a configuration other than the coplanar symmetric one, all that is necessary is a reinterpretation of the patterns shown in figures 6(*a*) and 12(*a*), for example, and of the dislocation arrival-time data. It can be shown (from (2) and (3)) that this reinterpretation involves only a linear transformation.

A way of generating a three-dimensional arrangement containing the essence of the three-dimensional case, but without the unhelpful complications of total generalisation, is to take the coplanar symmetric case and raise each of the original $\boldsymbol{k}$ vectors out of the plane by an equal angle θ. Using this configuration, we now reinterpret the pattern of trajectories calculated for the hyperbolic secant, say. The necessary transformation on the pattern in figure 6, which becomes a section through a three-dimensional wavefield perpendicular to the symmetry axis, is simply a radial expansion by a factor of sec θ. The time of arrival of a dislocation at a point on the trajectory surface at height h (above the plane through the origin perpendicular to the symmetry axis) is given by $t_d + (h \sin\theta)/c$, where t_d is the value computed for the coplanar case ($\theta = 0$). These results are easily obtained from equations (2) and (3). The most marked change that occurs when the $\boldsymbol{k}$ vectors are raised (that is, θ made non-zero) is to the shape

of the dislocation line embedded in the trajectory surface: rather than being straight and parallel to the symmetry axis, it becomes curved with a slope dependent on θ and on the local gradient of the dislocation arrival time across the trajectory. This can be explained as follows.

Referring to figure 15, consider the intersection of the trajectory surface with the plane perpendicular to the symmetry axis and containing the origin. At any point P on this line there is a time when the received signal is zero, as a result of the interference of three wavefronts, one from each pulse. This is the time of arrival t_d of the dislocation at P. The intersection of the three wavefronts describes a time-labelled line PR parallel to the symmetry axis. The speed along this line of the point of intersection is c cosec θ. Now, the phase relation between the three wavefronts remains constant (by definition) and, at the point of intersection, their amplitudes remain constant because the waves are plane and the group and phase velocities are identical. The dislocation condition is always satisfied, therefore, at the intersection point, and the speed of the dislocation line parallel to the symmetry axis must be c cosec θ. At a point Q a distance ds across the trajectory from P, the dislocation will result from the interference of three different wavefronts intersecting at a different time, $t_d + dt_d$, say. The time labels on the line described by the intersection of these three wavefronts will therefore be out of step by dt_d with those on the first. Now, because a dislocation line is the locus of points of zero amplitude at a given time, locally that locus will have a gradient of $-(dt_d/ds)(c \text{ cosec } \theta)$. Notice that in the coplanar case, where $\theta = 0$, the speed of the points of intersection (and, therefore, of the dislocation lines parallel to the symmetry axis) becomes infinite, as does the gradient of the dislocation line. However, when $\theta \neq 0$, the gradient depends on the rate of change of arrival time with distance s.

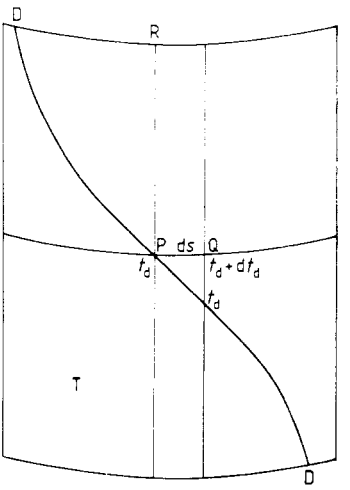

Figure 15. The trajectory surface T is part of a (non-circular) cylinder with generators parallel to the symmetry axis. At time t_d the dislocation line is DPD. At time $t_d + dt_d$ it has moved rigidly upwards to pass through Q.

Whether a wave dislocation line is edge or screw or mixed edge-screw depends on its direction relative to the local plane wave that it dislocates (Nye 1981). We shall take this to be the mean wavevector $\bar{\boldsymbol{k}}$ of the original beams. It follows that the dislocations in our model have an edge-screw nature dependent on their gradient.

Each dislocation line is curved, being pure screw at the edges of the trajectory surface ($t = \pm\infty$), where dt_d/ds is large, and mixed edge-screw towards the middle.

The motion of a dislocation line relative to the local plane wave determines its glide and climb (as in crystals glide and climb denote motion relative to the crystal lattice). Because the phase velocity of the mean wave is the same as the velocity of the dislocation lines along the symmetry axis, the dislocations in the symmetric case we are now considering neither glide nor climb: they are carried rigidly by the wave. In a more general three-beam configuration, however, $\bar{k}$ would not lie in the dislocation trajectories, and both climb and glide would be exhibited.

A common type of trajectory in the outer region is one that starts as being of two-beam character and, as it gets nearer the intermediate region, becomes influenced by the third beam. The perturbation from the third beam has two effects: the dislocation arrival time starts fluctuating as a function of distance along the trajectory and the trajectory itself becomes corrugated. In fact, the corrugations are in quadrature with the fluctuations and so the dislocation line is actually helical, the radius of the helix increasing as the intermediate region is approached. We show in appendix 2 that this is an extension to pulses of a general result for continuous waves, that straight nulls become helical when perturbed by a weak plane wave (Berry *et al* 1979).

Although we have discussed in detail only one three-dimensional configuration of beams, this simple symmetrical case contains all the significant aspects of a general three-dimensional configuration. Any other wavefield consisting of three beams of plane waves can be investigated using the appropriate linear transformation on the same computed results.

9. Conclusions

A model wavefield has been presented which, when pulse modulated, contains wavefront dislocations displaying diverse behaviour, including examples of edge, screw and mixed edge-screw dislocations, gliding and climbing in very general ways. However, all models are in some sense special, limiting the variety of behaviour of their dislocations. In the three-beam model the most striking special property is the way saddle points in M_0 appear to pin trajectories, an effect seen only at high delay-bandwidths when the trajectories are long enough to extend that far. Although in this model we expect the potential trajectories of the Wright and Nye small-bandwidth theory to contain the saddles, the reason why the trajectories computed for large bandwidths are similarly constrained is not yet understood.

The simplicity of the computation necessary to calculate the trajectories has allowed a detailed comparison of the exactly computed dislocation behaviour with the predictions given by the small-bandwidth theory, for several different bandwidths and envelope shapes. The comparisons show good agreement. The validity of the Wright and Nye local theory, applicable only near the CW nulls, has also been demonstrated.

For larger bandwidths the exact computations reveal new behaviour. As the delay-bandwidth increases, the ends of the trajectories for hyperbolic secant pulses first join together, and then the resulting ring trajectories develop cusps and loops which enable them to hook up with their neighbours. For Lorentzian pulses the behaviour is more complicated. At lower delay-bandwidths the dislocations travel in long loops that begin and end on CW nulls. As the delay-bandwidth increases the ends of the loops join together to give intersecting trajectories of two kinds: those which

include the CW nulls and have large dislocation arrival times, and those where the dislocations have higher visibility and smaller arrival times. At still larger delay-bandwidths the trajectories develop cusps and loops and hook up with their neighbours in the way already seen for the hyperbolic secant pulse. A fuller account of the detailed behaviour of the dislocations in the three-beam model has been given by Nicholls (1984).

Appendix 1. The amplitude and phase of the continuous-wave pattern produced by three beams

In this appendix we discuss the continuous wave pattern whose complex amplitude a is given by equation (7). As pointed out in § 3, this can be regarded as a three-dimensional pattern either in ϕ space or in $\boldsymbol{r}$ space, the two representations being linearly related by equations (8). Figures 3 and 16(a) display the two-dimensional section by the reference plane $\phi_1+\phi_2+\phi_3=0$ in ϕ space or $(\boldsymbol{k}_1+\boldsymbol{k}_2+\boldsymbol{k}_3)\cdot\boldsymbol{r}=0$ in $\boldsymbol{r}$ space. These diagrams use the plotting convention described in §§ 2 and 3 and are therefore undistorted pictures for the special case where the three beams are coplanar and at 120° to one another.

The nulls shown by the contours of the amplitude pattern (figure 3) appear in the phase plots (figure 16(a)) as points where the contours of equal phase all come together radially. The smallest (primitive) unit cell for amplitude (broken line in figures 3 and 16(a)) contains two nulls, one maximum and three saddle points. The smallest unit cell for phase (full line in figure 16(a)) is three times larger.

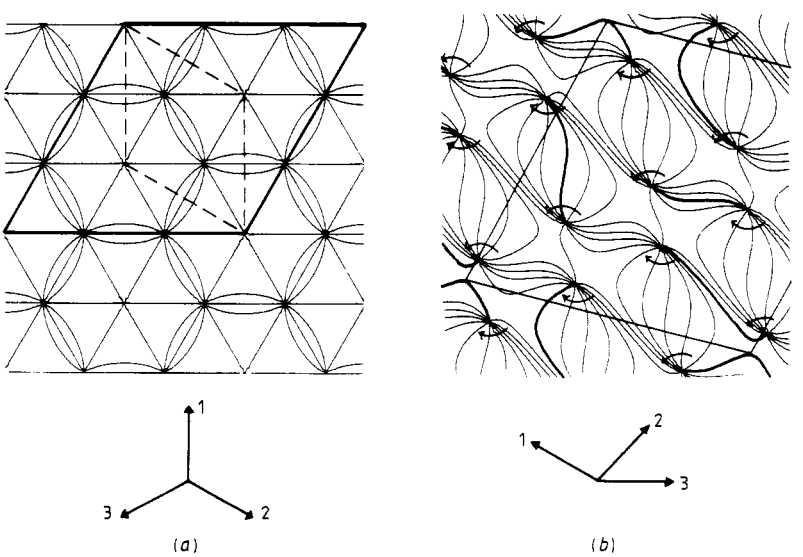

Figure 16. Contours of equal phase in the CW three-beam interference pattern. (a) The reference plane. (b) The lattice plane in ϕ space defined by $3\phi_1-2\phi_2+4\phi_3=0$; one way of obtaining this pattern would be by the coplanar arrangement of beams shown below. A datum contour is indicated by the bolder line and the phase changes in the direction shown by the arrows. The repeating pattern of the nulls is clearly seen and part of a primitive unit cell for phase, containing ten nulls, is indicated.

As pointed out in § 3, the amplitude pattern, i.e. the pattern of M_0, is essentially two dimensional, being constant on lines parallel to $\phi_1 = \phi_2 = \phi_3$, and therefore it can be fully shown on a plane diagram. For a general set of beam directions the amplitude pattern on any transverse plane (that is, not containing the pattern axis) is simply a linear distortion of the one shown.

The phase distribution, however, is three dimensional, although its variation parallel to the line $\phi_1 = \phi_2 = \phi_3$ is merely linear, by equation (9). This means that on planes inclined to the reference plane the contours of equal phase will not be just a linear distortion of those shown but will have different forms. An interesting consequence of this is that on the reference plane (figure 16(a)) there are places where the phase contours cross in threes to give monkey saddles. The reference plane is exceptional in this respect; on other lattice planes the phase saddles are of the usual kind, as illustrated in figure 16(b).

In ϕ space the phase distribution of a always possesses a three-dimensional lattice (counting phase $\phi + 2\pi$ as equivalent to phase ϕ) and in general this maps into a three-dimensional lattice in $\boldsymbol{r}$ space. However, there is an exception when the beams are coplanar with an irrational relation between their k vectors

$$p\boldsymbol{k}_1 + q\boldsymbol{k}_2 + s\boldsymbol{k}_3 = 0. \tag{A1.1}$$

In this case the whole of $\boldsymbol{r}$ space maps into the single plane

$$p\phi_1 + q\phi_2 + s\phi_3 = 0$$

in ϕ space. Being irrational, this plane in ϕ space does not possess a lattice and so neither does the three-dimensional phase distribution in $\boldsymbol{r}$ space; perpendicular to the plane of the beams the phase is constant and in the plane of the beams it is not periodic. This restriction does not apply to the amplitude pattern, which is always periodic, because in both ϕ space and $\boldsymbol{r}$ space it is always effectively two dimensional, being invariant in the direction $\phi_1 = \phi_2 = \phi_3$ or $\boldsymbol{k}_1 \cdot \boldsymbol{r} = \boldsymbol{k}_2 \cdot \boldsymbol{r} = \boldsymbol{k}_3 \cdot \boldsymbol{r}$. However, although the distribution of phase in the plane of the beams does not strictly possess a lattice, its contour pattern still displays the periodicity of the amplitude pattern in a restricted sense. If the contour interval is $2\pi/n$, where n is an integer, the pattern of lines never repeats, because of the irrationality of $p:q:s$, but nevertheless the *continuous* field of contour directions that it represents, divested of contour labels, is periodic. The plane in ϕ space chosen for figure 16(b) is rational, but the large unit cell indicates the approach to irrationality.

Appendix 2

Berry *et al* (1979) have shown that, for continuous waves, a straight null line becomes helical when perturbed by a weak plane wave. We now extend this result to the general case of time-dependent dislocations. A general wavefield can be represented by the wavefunction $\psi(\boldsymbol{r}, t) = F(\boldsymbol{r}, t) \exp \mathrm{i}(\boldsymbol{k}_m \cdot \boldsymbol{r} - \omega_0 t)$, where F is a complex envelope function and $\boldsymbol{k}_m$ the wavevector of a factored-out plane wave. The only constraint on $\psi(\boldsymbol{r}, t)$ is that it satisfies the scalar wave equation. If we make a local expansion of the envelope function in the neighbourhood of the dislocation line, it can be truncated to first order, as this is sufficient to contain a dislocation's wave structure, provided it is isolated (Nye 1981). Hence

$$\psi(x, y, z, t) = \{(a + \mathrm{i}b)(x - vt) + (c + \mathrm{i}d)y\} \exp[\mathrm{i}(k_x x + k_y y + k_z z - \omega_0 t)] \tag{A2.1}$$

where k_x, k_y, k_z are the components of $\boldsymbol{k}_m$, and a, b, c, d, v are real constants, and where Oz and Ox have been chosen tangent to the dislocation line and trajectory surface respectively. By equating the envelope in (A2.1) to zero (the dislocation condition), and separating the real and imaginary parts, the dislocation can be seen to be travelling with a speed v along the x axis; at $t = 0$ the dislocation passes through the origin. The trajectory of the dislocation is the plane $y = 0$. We now perturb ψ using a plane wave with wavevector $\boldsymbol{k}'$, frequency ω_0 and (small) amplitude ε. The perturbed wavefield is given by

$$\psi'(x, y, z, t) = E(x, y, t) \exp[\mathrm{i}(k_x x + k_y y + k_z z - \omega_0 t)]$$
$$+ \varepsilon \exp[\mathrm{i}(k'_x x + k'_y y + k'_z z - \omega_0 t + \delta)] \tag{A2.2}$$

where E is the envelope function for the unperturbed wave (from (A2.1)), k'_x, k'_y, k'_z are the components of $\boldsymbol{k}'$, δ is an arbitrary phase difference between the unperturbed and perturbing waves and ε is real. Defining $\Delta\boldsymbol{k} = \boldsymbol{k}_m - \boldsymbol{k}'$, (A2.2) may be rewritten as

$$\psi' = \{E \exp[\mathrm{i}(\Delta\boldsymbol{k} \cdot \boldsymbol{r})] + \varepsilon \exp(\mathrm{i}\delta)\} \exp[\mathrm{i}(\boldsymbol{k}' \cdot \boldsymbol{r} - \omega_0 t)]$$

and the condition for the perturbed dislocation becomes

$$E \exp[\mathrm{i}(\Delta\boldsymbol{k} \cdot \boldsymbol{r})] + \varepsilon \exp(\mathrm{i}\delta) = 0.$$

This condition is satisfied when the amplitudes of E and ε are equal and when the phases of the two terms differ by π, i.e.

$$EE^* = \varepsilon^2 \tag{A2.3a}$$

and

$$\tan^{-1}\{[b(x - vt) + dy]/[a(x - vt) + cy]\} + \Delta\boldsymbol{k} \cdot \boldsymbol{r} - \delta - \pi = 0 \tag{A2.3b}$$

where E^* is the complex conjugate of E. In full, the amplitude condition (A2.3a) is

$$(a^2 + b^2)(x - vt)^2 + y^2(c^2 + d^2) + 2y(x - vt)(bd + ac) - \varepsilon^2 = 0 \tag{A2.4}$$

which represents an ellipse lying in the xy plane and moving along the x axis at the unperturbed dislocation's speed v. From (A2.4) the size of the ellipse is proportional to ε. For sufficiently small ε, therefore, the contribution to the phase variation across the ellipse from the second (plane-wave) term in (A2.3b) can be assumed negligible compared with the contribution from the arctangent term. The phase condition (A2.3b) then becomes

$$\tan^{-1}\{[b(x - vt) + dy]/[a(x - vt) + cy]\} + \Delta k_z z - \delta - \pi = 0. \tag{A2.5}$$

At a fixed time, for any given z plane there is only one point on the ellipse where (A2.5) is satisfied and that point progresses around the ellipse as the z plane is changed. Thus the perturbed dislocation line takes the form of a helix with pitch $2\pi/\Delta k_z$. The smallest pitch possible is with $\boldsymbol{k}_m$ and $\boldsymbol{k}'$ antiparallel and lying in the z direction. With our definition of $\boldsymbol{k}_m$ for the three-beam model the largest value of $|\boldsymbol{k}_m|$ is k and the smallest pitch is $\frac{1}{2}\lambda$.

References

Berry M V, Nye J F and Wright F J 1979 *Phil. Trans. R. Soc.* A **291** 453-84
Humphrey V F 1980 *PhD Thesis* University of Bristol
Nicholls K W 1984 *PhD Thesis* University of Bristol
Nicholls K W and Nye J F 1986 *J. Phys. A: Math. Gen.* **19** 375-83
Nye J F 1981 *Proc. R. Soc.* A **378** 219-39
Nye J F and Berry M V 1974 *Proc. R. Soc.* A **336** 165-90
Wright F J and Berry M V 1984 *J. Acoust. Soc. Am.* **75** 733-48
Wright F J and Nye J F 1982 *Phil. Trans. R. Soc.* A **305** 339-82